Journal of
Materials Chemistry C

RSCPublishing

PAPER

View Article Online
View Journal | View Issue

Cite this: *J. Mater. Chem. C*, 2013, **1**, 2875

Synthesis of nonstoichiometric zinc ferrite nanoparticles with extraordinary room temperature magnetism and their diverse applications†

Yang Yang,[a] Xiaoli Liu,[a] Yong Yang,[a] Wen Xiao,[a] Zhiwei Li,[b] Desheng Xue,[b] Fashen Li[b] and Jun Ding*[a]

Received 5th December 2012
Accepted 27th February 2013

DOI: 10.1039/c3tc00790a

www.rsc.org/MaterialsC

A series of nonstoichiometric zinc ferrite ($Zn_dFe_{3-d}O_4$) nanoparticles with Zn-dopant concentration *d* ranging from 0 to 0.5 was synthesized *via* thermal decomposition route employing oleic acid as surfactant. The zinc dopant concentration was controlled by the ratio of Zn/Fe precursors. High room temperature saturation magnetization of 110 emu g^{-1} was obtained for large Zn ferrite particles (more than 100 nm) with nominal composition of $Zn_{0.468}Fe_{2.532}O_4$. The origin of the extraordinary magnetic property was revealed as the Zn substitution of Fe atoms at the tetrahedral site (A site) in the spinel magnetite phase. It was found that the precursor/surfactant ratio was an important parameter for the control of the shape and size of as-synthesized Zn ferrite particles. The details were investigated through a series of experimental work. Size-dependent applications, such as radar absorption and magnetic fluid hyperthermia, were further studied. Both applications required magnetic particles with high saturation magnetization, hence our samples displayed advantages over Fe_3O_4 magnetite nanoparticles. Especially for magnetic fluid hyperthermia, 26 nm Zn ferrite nanoparticles coated by P-mPEG polymer showed superior biocompatibility and heating efficiency, implying the potential usefulness to *in vivo* cancer therapy.

Introduction

Over the past decades, magnetic spinel ferrites [M(II)Fe(III)$_2$O$_4$; M represents Co, Mn, Ni, Zn or Fe, *etc.*] have attracted considerable research interest for their wide range of technological applications in magnetic recording, microwave technology, catalytic and biomedical fields.[1–5] Spinel has a face-centred cubic structure with the oxygen anions arranged in a cubic closed-packed lattice. The metal cations fill either the tetrahedral or octahedral interstices, resulting in normal structure when M occupies the tetrahedral (A) sites and inverse structure when M occupies the octahedral (B) sites. Also, intermediate cases exist where the cations distribute at both sites. The formula is commonly described as $(M_{1-x}Fe_x)[M_xFe_{2-x}]O_4$, where the round and square brackets refer to A sites and B sites, respectively. *x* stands for the inversion degree, defined as the fraction of A sites occupied by Fe^{3+} cations. Magnetically, the origin of net moment in a unit formula (u.f.) of the spinel structure is from the arithmetic difference of the magnetic moments at A sites (upwards) and at B sites (downwards).[6] Hence the cation distribution exerts a decisive influence on the magnetic properties of spinel ferrites,[7–9] such as blocking temperature, magnetization and AC magnetic susceptibility. The control of cation distribution provides a means to tailor their properties. Theoretically, the preferable distribution of various metal cations in spinel ferrites could be predicted by taking the crystal field stabilization energy and ionic radius into consideration.[10] The results based on a normalized ion energy method[11] show that Fe^{2+}, Co^{2+} and Ni^{2+} tend to locate at B sites to form inverse spinel structures, while Zn^{2+} and Mn^{2+} tend to locate at A sites to form normal spinel structures.

$ZnFe_2O_4$ is a typical representative of normal spinel structure, in which all nonmagnetic Zn^{2+} cations and magnetic Fe^{3+} cations are located at A sites and B sites, respectively. Bulk $ZnFe_2O_4$ commonly shows paramagnetism at room temperature.[12,13] When the particle size enters the nanoregime, ferrimagnetism has been observed.[14,15] The major origin of the observed ferrimagnetism is the redistribution of Zn atoms at A and B sites,[16] which is greatly influenced by the synthetic approach.[17] Various methods, such as high temperature calcination, ball milling, coprecipitation, combustion, sol–gel, hydrothermal and thermal decomposition routes,[18–23] have been developed to synthesize Zn ferrite. The calcination route and

---

[a] *Department of Materials Science & Engineering, National University of Singapore, Singapore 119260, Singapore. E-mail: msedingj@nus.edu.sg; Fax: +65 6776 3604; Tel: +65 6516 4317*

[b] *Institute of Applied Magnetics, Key Lab for Magnetism and Magnetic Materials of the Ministry of Education, Lanzhou University, Lanzhou 730000, Gansu, People's Republic of China*

† Electronic supplementary information (ESI) available: SEM images of Zn ferrite nanoparticles with irregular shapes, resulting from the overuse of precursors. See DOI: 10.1039/c3tc00790a

ball milling method are favourable to produce a highly crystalline nanostructure, but always lead to agglomeration and/or large size distribution. By contrast, chemical syntheses are preferred due to the better control over the shape and size for particle synthesis. The hydrothermal method was employed by Li *et al.*[24] to produce Zn ferrite nanoparticles (NPs). When the Zn dopant concentration reached 0.33, room temperature saturation magnetization (M_s) was around 80 emu g^{-1}. Liu *et al.*[25] obtained $Zn_{0.2}Fe_{2.8}O_4$ particles by coprecipitation technique and obtained a saturation magnetization of 80.93 emu g^{-1}. The inconsistency in the composition and the resultant saturation magnetization might be due to the disordered distribution of Zn atoms at the interstitial sites. Most of the studies[26,27] have focused on the ferrimagnetism of Zn ferrite particles with sizes less than 50 nm. However, it is not easy to control the distribution of Zn atoms at either A sites or B sites because of the disorder induced by the high surface energy of small particles.[28] In this work, uniform Zn ferrite particles with size above 100 nm were prepared using thermal decomposition method. This method is appropriate to synthesize nanoparticles on the large scale.[29] The control over the size and shape of the as-synthesized Zn ferrite particles was investigated. Large Zn ferrite particles show a high room temperature saturation magnetization of 110 emu g^{-1}, which is significantly higher than bulk Fe_3O_4 ($\sim$90 emu g^{-1}).[30] The results revealed that the room temperature ferrimagnetism is mainly caused by the distribution of Zn atoms at only A sites.

Ferrites are of great interest in electromagnetic applications because they can absorb electromagnetic radiation in microwave bands.[31] Compared with the traditional Zn ferrite, the as-synthesized particles exhibit promising magnetic property, which is attractive to investigate their performance of radar absorption. To date, there are very few reports available regarding the radar absorption by using pure zinc ferrite particles. Srivastava *et al.*[32] reported the permeability spectrum of zinc ferrite prepared from a high temperature calcination process in the 1970s. Although high room temperature M_s was observed, the resonant frequency appeared at only several tens megahertz. And the inhomogeneous particle sizes limited its application. From the results revealed by Yan and Li *et al.*,[33,34] we can see that the shape and size of zinc ferrite NPs are well controlled with the development of chemical synthesis, making high M_s zinc ferrite more promising as a radar absorbing material. To enrich the study on this aspect, the radar absorbing performance of the as-synthesized Zn ferrite particles in our work was also investigated by both experimental measurement and computational study.

Another electromagnetic application of the as-synthesized zinc ferrite is magnetic fluid hyperthermia for cancer therapy, which also requires magnetic NPs with relatively high saturation magnetization as well as good biocompatibility (non-toxicity), chemical stability, uniformity in size and good dispersibility in aqueous media.[35] In order to demonstrate the related properties, zinc ferrite NPs with size corresponding to the superparamagnetic regime were also prepared by thermal decomposition method and the particle surface was modified by coating with P-mPEG for further investigation. Criteria such as effective specific absorption rate and *in vitro* cytotoxicity are within the scope of this study and were investigated.

Experimental section

Materials

Benzyl ether (98%), oleic acid ($\geq$99%), iron(III) acetylacetonate ($Fe(acac)_3$, $\geq$97.0%) and zinc acetylacetonate hydrate ($Zn(acac)_2 \cdot xH_2O$), used as starting materials for the synthesis of zinc ferrite NPs (NPs), were purchased from Sigma-Aldrich. Phosphorylated-mPEG (P-mPEG) was prepared using methoxy poly(ethylene glycol) (mPEG; $M_w = 2000$ Da) and phosphorus(V) oxychloride ($POCl_3$, 99%) purchased from Sigma-Aldrich. Concentrated nitric acid (65%) was purchased from VWR for the preparation of samples for ICP measurement. Hexane (95%) and chloroform ($\geq$99%) were used as solvents for dispersion of as-synthesized NPs, both also from Sigma-Aldrich.

Synthesis of large size zinc ferrite nanoparticles (NPs)

Zinc ferrite NPs were fabricated *via* thermal decomposition route, which was redesigned based on the previous synthesis of octahedral magnetite NPs reported by our group.[36] In a typical reaction of zinc ferrite sample ZF3, 12 mmol $Fe(acac)_3$ and 6 mmol $Zn(acac)_2 \cdot xH_2O$ were dissolved in benzyl ether (20 mL). Oleic acid (28 mmol) was added as surfactant to control the particle growth and prevent interparticle aggregation. The mixture was heated to 120 °C and kept for 30 min to eliminate the bound water from precursors and finally heated to 280 °C at a rate of 8 °C min^{-1} to reflux the mixture for 30 min. The gray-black precipitates were collected by magnetic separation after the mixture was cooled down to ambient temperature naturally, and then washed by organic solvent (hexane) several times. A series of samples from ZF0 to ZF7 were obtained by only adjusting the amount of zinc precursor from 0 to 15 mmol while keeping the amount of iron precursor at 12 mmol. Such a kind of adjustment is aimed at synthesizing large zinc ferrite particles with different zinc dopant concentrations. Table 1 lists the amounts of starting materials and the resulting compositions.

Synthesis of small size zinc ferrite nanoparticles (NPs)

In this work, the size of as-synthesized Zn ferrite NPs could be purposely decreased by scaling down the precursors. Take sample ZF3 for example, of which the composition is $Zn_{0.387}Fe_{2.613}O_4$. When the amounts of iron and zinc precursors were scaled down to 8 mmol and 4 mmol, respectively, zinc ferrite with a relatively smaller size of 26.5 nm could be successfully produced. The sample was labeled differently by following with a number related to the particle size, such as ZF3_26.5, ZF3_13.4. Although the particle size was reduced by decreasing the concentration of used precursors, the composition of these samples changed little owing to the fixed ratio of Zn/Fe precursors. Hence, the developed method succeeded to control the particle size as well as the composition of as-synthesized zinc ferrite NPs.

Table 1 The amounts of starting precursors and some relevant experimental results[a]

Sample no.	$Fe(acac)_3$ (mmol)	Molar ratio of Zn/Iron precursors	Resulting composition	M_s (emu g^{-1})	Lattice constant (Å)
ZF0	12	0	Fe_3O_4	85.2	8.396
ZF1	12	0.17	$Zn_{0.189}Fe_{2.811}O_4$	97	8.403
ZF2	12	0.33	$Zn_{0.290}Fe_{2.710}O_4$	106.8	8.408
ZF3	12	0.5	$Zn_{0.387}Fe_{2.613}O_4$	107.2	8.411
ZF4	12	0.67	$Zn_{0.468}Fe_{2.532}O_4$	109.7	8.418
ZF5	12	0.83	$Zn_{0.522}Fe_{2.478}O_4$	104.4	8.420
ZF6	12	1	$Zn_{0.524}Fe_{2.476}O_4$	99.8	8.415
ZF7	12	1.25	$Zn_{0.527}Fe_{2.472}O_4$	94.2	8.410

[a] 28 mmol oleic acid and 20 mL benzyl ether were used for all the reactions.

Synthesis of P-mPEG modified zinc ferrite NPs

The as-synthesized zinc ferrite NPs are water insoluble due to the hydrophobic oleyl group on the NP surface. For phase transfer into aqueous medium, P-mPEG was employed as the hydrophilic coating through a ligand exchange reaction. The detailed procedure could be found in our previous publication,[37] in which P-mPEG coated Fe_3O_4 NPs were studied as the hyperthermia agent. Here the procedure is briefly introduced regarding the current study. Before the surface coating process, P-mPEG was prepared by reacting $POCl_3$ with mPEG (M_w = 2000 Da) as previously described.[38] Then sufficient P-mPEG was added to a chloroform solution (20 mL) of well dispersed, as-synthesized zinc ferrite NPs (5 mg). The mixed solution was shaken for 2 h at ambient temperature by using an IKS Mechanical Shaker (HS/KS260 control). The final solution after reaction was evaporated under a flow of argon and then dried under vacuum for 2 days. The collected dry NPs were further dispersed in water (5 mL) and the solution was centrifuged to remove the extra polymer. The P-mPEG coated zinc ferrite NPs remained dispersed in the supernatant after being centrifuged at 3000 rpm for 10 min, and therefore the supernatant was collected and stored for future use.

Structure and morphology detection

X-ray diffraction (XRD; Bruker, Advance D8) was performed to detect the phase of as-synthesized samples. Rietveld refinements of XRD powder patterns were performed with the Generalized Structure Analysis System (GSAS), along with the graphical user interface EXPGUI. Field-emission scanning electron microscopy (FESEM; Zeiss Supra 40) and the attached energy-dispersive X-ray spectroscopy (EDX) were employed to detect the morphology and composition of as-synthesized zinc ferrite NPs, respectively. Transmission electron microscopy (TEM, JEOL-2010 at 200 kV) was performed to acquire high resolution TEM (HRTEM) images. The hydrodynamic diameters were evaluated from dynamic light scattering (DLS) measurements using a Malvern Zetasizer Nano-ZS. FT-IR spectra of Zn ferrite nanoparticles were recorded using a Varian 3100 FT-IR (Excalibur series) spectrophotometer in the range 4000–400 cm^{-1} at a resolution of 4 cm^{-1}.

Magnetic property characterization

Magnetic properties of as-synthesized samples were evaluated using a vibrating sample magnetometer (VSM; Lakeshore, Model 7404) and superconducting quantum interference device (SQUID) system (Quantum Design, MPMS, XL-5). The magnetic structure was determined by zero field Mössbauer spectra, which were recorded at room temperature, using a conventional constant acceleration spectrometer with a γ-ray source of 57Co/Pd embedded in palladium matrix. A spectrum of bcc-Fe was used for the calibration. Spectra of as-synthesized zinc ferrite nanocrystals were fitted based on Lorentzian site analysis by RECOIL software.

Microwave absorption measurement

For microwave measurements, zinc ferrite NPs were uniformly mixed with paraffin wax at a volume concentration of 1 : 5. The mixture was then pressed into toroids with an outer diameter of 6.9 mm and an inner diameter of 3 mm using a stainless steel mould under a pressure of 1 MPa. The complex permeability ($\mu_r = \mu' - j\mu''$) and permittivity ($\varepsilon_r = \varepsilon' - j\varepsilon''$) of the composites were measured over the frequency range of 0.1–18 GHz using a network analyzer (Agilent PNA 8363B). The reflection loss (RL) was calculated from the measured μ_r and ε_r at a given frequency and absorber thickness t according to the following equations:[39]

$$\mathrm{RL} = 20\log|(Z_{\mathrm{in}} - Z_0)/(Z_{\mathrm{in}} + Z_0)| \tag{1}$$

$$Z_{\mathrm{in}} = Z_0\sqrt{\mu_r/\varepsilon_r}\tanh\{j(2\pi ft/c)\sqrt{\mu_r\varepsilon_r}\} \tag{2}$$

where Z_{in} is the input impedance at absorber surface, Z_0 is the impedance of air, f is the frequency of incoming microwave, and c is the velocity of light.

ICP-MS analysis

Both the iron and zinc concentrations of the ferrofluid samples (water suspension of zinc ferrite NPs) were determined by Inductively Coupled Plasma Mass Spectrometer (ICP-MS) analysis. A known volume of ferrofluid sample was put into a glass test tube and 2 mL concentrated nitric acid was added. The tube was heated to 80 °C for 45 min and the sample was analyzed using ICP-MS (Agilent ICP-MS 7500 Series) after sufficient dilution with Milli-Q water. The analysis of samples was done in comparison with the ICP-MS standard (Sigma). The composition of as-synthesized zinc ferrite NPs was also estimated based on ICP results.

In vitro cytotoxicity study

The cytotoxicity of the magnetic NPs system was detected by Cell Counting Kit-8 (CCK-8) assay. The operation procedure of CCK-8 test is as follows. Prior to the cytotoxicity test, MCF-7 mammalian breast cancer cells were trypsinized and washed (by centrifugation) and re-suspended in the culture growth medium (DMEM/10%FBS). MCF-7 cells were seeded in a 96-well plate at the density of 5×10^4 viable cells per well using DMEM containing 10% FBS, and incubated for 24 h to allow cell attachment. The medium was removed and then replaced with fresh medium. To each well, 100 μL of the modified NP suspension at concentrations of 5 to 200 μg mL^{-1} Fe were added and incubated for 24 h. Wells without NPs treatment were used as controls. To test for the cell viability, 10 μL CCK-8 solution was added to each well and the 96-well plates were further incubated for another 4 h before the absorbance readings were taken. The absorbance readings were analysed using a microplate reader (FlUOstar OPTIMA, Germany) at 450 nm as reference wavelength. The cell viability was then calculated by:

$$\%\text{Cell viability} = \frac{\text{Aborbance of sample well}}{\text{Absorbance of control well}} \times 100 \quad (3)$$

Magnetic hyperthermia study

The ability of heat dissipation of magnetic NPs is usually evaluated in terms of specific absorption rate (SAR), which is calculated by the following equation:

$$\text{SAR} = C\frac{\Delta T}{\Delta t}\frac{1}{m_{\text{Fe}}} \quad (4)$$

where C is the specific heat of the medium ($C_{\text{water}} = 4.18$ J g^{-1} °C^{-1}), $\Delta T/\Delta t$ is the initial slope of the time-dependent temperature curve and m_{Fe} is the weight fraction of Fe in the medium. However, it should be noted that the obtained SAR values in W g^{-1} could not fully express the true heat capacitance of samples because the heat dissipation is also influenced by the frequency and square of the magnetic field strength used during the measurements. For example, the frequency was 240 kHz and the amplitudes of AC magnetic field (AFM) were adjusted to be 12.1 kA m^{-1}, 16.8 kA m^{-1} and 24.2 kA m^{-1} in the current study. Under these different conditions the temperature rise of 1 mL aqueous suspension of the modified zinc ferrite NPs with time was recorded with the software provided by the equipment (Ambrell, Easy Heat 4.2–10 kW). To characterize the heat capacitance of magnetic particles for hyperthermia more clearly, a developed definition of effective specific absorption rate (ESAR)[40] was proposed and expressed as the SAR value (W g^{-1}) divided by $H^2 \times f$, where H and f are the amplitude and frequency of applied AFM.

Results and discussions

Synthesis and characterizations on large zinc ferrite NPs

Uniform Zn ferrite NPs were prepared *via* thermal decomposition of iron and zinc precursors in the solvent of benzyl ether. For all experiments, the same amounts of oleic acid (28 mmol) and benzyl ether (20 mL) were used. Table 1 lists the samples in this work (ZF0 to ZF7) with different amounts of starting precursors. Actually, ZF0 is pure Fe_3O_4 without any zinc dopant. Variations in the morphology of as-synthesized samples could be observed from SEM images as shown in Fig. 1a–f. When the amount of zinc precursor is around 4 mmol or less, octahedral shaped particles are formed, such as samples ZF1 and ZF2. With increasing the zinc precursor to 6 mmol (ZF3) and 8 mmol (ZF4), well faceted polyhedral crystallites are formed. When 10 mmol of zinc precursor is used, nonuniform particles including large cubes and some small ones are obtained, as shown for the sample ZF5. Based on the previous study on the formation mechanism of octahedral magnetite particles,[36] we have learned that oleic acid acts as both reducing agent and stabilizer in the synthesis process and the precursor/surfactant ratio is crucial to the morphology. Further increase of zinc precursor will result in a deficiency in the surfactant, which makes it hard to stabilize all formed nuclei homogeneously. That is why the samples ZF5 and ZF6 seem irregular and nonuniform. Hence, there is a limitation set by the ratio of precursor to surfactant. Only if the ratio is less than 0.85, Zn ferrite NPs with defined shapes could be obtained. This could be further verified by sample ZF7, which was prepared by using precursors amounting to 27 mmol. We could find many heterogeneous particles included in the SEM image, seen from Fig. S1 (ESI†).

The formation of various shapes may rely on the ratio of precursor/surfactant, which is the only modified parameter in the experiment. Hence, the mechanism is proposed as the following based on the observed results. The previous works on the shape control of particles of Au,[41] In_2O_3[42] as well as iron oxides[43,44] have indicated that the selective adsorption of surfactant on a particular surface is mostly dependent on the surface energy. The high-index crystallography planes usually possess higher surface energy. As a result, the particles tend to

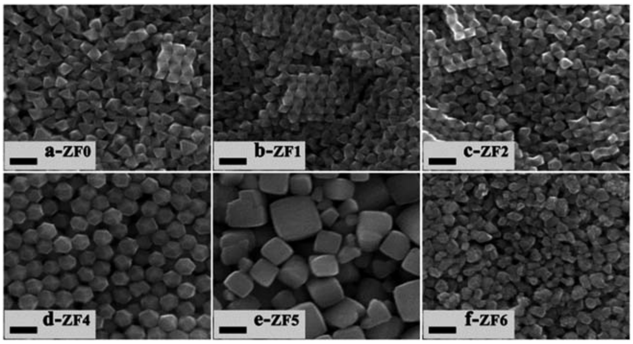

Fig. 1 (a–f) SEM images of as-synthesized samples. All the scale bars stand for 200 nm.

be surrounded by low-index planes, such as the {111}, {110} and {100} planes in face-centered cubic structured materials. Our previous report[36] on the synthesis of octahedral Fe_3O_4 particles has also revealed that the precursor/surfactant ratio is a decisive factor in the formed particle shape. The particle shapes are closely related to these crystallographic planes that enclose the particles. The octahedral shape has eight faces enclosed by {111} planes and the cubic shape has six faces enclosed by {100} planes. The microstructure features of particles with different shapes were characterized by HRTEM images. The crystalline directions were judged from the measured lattice space values, as labelled on the HRTEM images. The lattice spacings in Fig. 2d–f were measured at 0.48 nm, 0.24 nm and 0.30 nm, which are very close to the standard lattice spacings of {111}, {222} and {110} planes for the cubic spinel structure. Schematic drawings are shown in Fig. 2 to present three different shapes, including octahedron, polyhedron and cube, which were displayed by the as-synthesized Zn ferrite NPs. The polyhedral shape in this work is a kind of truncated octahedron. The excellent stabilizing function of oleic acid is due to the existence of the carboxylic group, as reported,[45] which always binds to certain crystal faces with a nonpolar tail group and hinders the growth in the direction normal to the bound faces. The surface energy is a key factor for the selective adsorption of stabilizer. The {111} planes possess the lowest surface energy,[46] hence the octahedron is much easier to form compared with the cube shape. In our work, octahedral zinc ferrite NPs are observed when the precursor/surfactant ratio is below 0.58. This is in agreement with Yang's[47] point that the presence of excess oleic acid will facilitate the growth of ⟨100⟩ over ⟨111⟩ direction, resulting in the formation of octahedral NPs. When the ratio is above 0.72, oleic acid tends to stabilize on the surface of (100) rather than (111), leading to a faster growth in the ⟨111⟩ direction and forming cubic NPs. The polyhedral NPs are formed as the ratio of precursor/surfactant is within the range of 0.6 to 0.75, resulting from competing growth in the ⟨100⟩ and ⟨111⟩ directions during the formation of zinc ferrite NPs. Although the shape induced performance is not in the scope of this study, the proposed formation mechanism of varying shapes is expected to be helpful to the further application of the developed method.

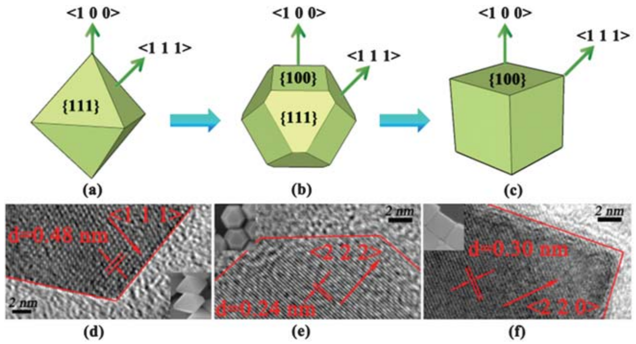

Fig. 2 Schematic drawings for different shapes of Zn ferrite NPs: (a) is for octahedron formed at low precursor/surfactant ratio (0.42–0.58); (b) is for polyhedron (truncated octahedron) formed at medium ratio (0.58–0.72) and (c) is for cube formed at high ratio (0.72–0.78). When the ratio is over 0.78, irregular particles will be obtained. The precursors include $Fe(acac)_3$ and $Zn(acac)_2$. (d)–(f) High resolution TEM images for different shapes. The insets are SEM images for octahedral, polyhedral and cubic particles, respectively.

It is worth noting that an increase of the zinc precursor used will not determine the obtained particle size. It is the amount of Fe precursor that is decisive to the particles size. When the amount of iron precursor is adjusted to be 12 mmol, all the produced samples are with similar sizes above 100 nm, which are in the bulk size regime. Based on our observation, $Zn(acac)_2 \cdot xH_2O$, as a secondary precursor, does affect the synthesis process in two manners. One is the effect on the ratio of precursor to surfactant, resulting in a morphology variation as explained above. The other is the effect on the ratio of Zn to Fe precursors, which further induces different compositions of the as-synthesized zinc ferrite NPs. The yielded compositions of as-synthesized samples were detected by EDX and ICP-MS. The obtained results from EDX and ICP-MS match well with each other. As listed in Table 1, there exists a discrepancy between the starting ratio of Fe to Zn precursors and the final ratio of iron to zinc concentrations in all samples. Obviously, the as-synthesized zinc ferrite NPs are nonstoichiometric, given as a formula of $Zn_dFe_{3-d}O_4$, where d represents the atomic concentration of zinc atoms. As listed in Table 1, the d value increases gradually with the amount of zinc precursor, reaches a saturation d value of *ca.* 0.52, as indicated by EDX results of sample ZF5 and ZF6. Even if the zinc precursor is increased to 15 mmol (ZF7), the d value is no more than 0.53.

The crystallographic information of the as-synthesized zinc ferrite NPs with different compositions was studied by XRD (Fig. 3a). All diffraction peaks match better with the standard Fe_3O_4 diffraction data (JCPDS no. 88-0135) than zinc ferrite data, this may be due to the low doping concentration of Zn atoms. Although the zinc dopant concentration varies between 0 and 0.527, the pure spinel cubic structure is shown by all the samples. According to Rietveld refinements of XRD patterns, the obtained lattice constants increase gradually with the zinc dopant concentrations, reaching a maximum value when Zn dopant concentration is 0.522 for sample ZF5. The change in lattice constant induced by the Zn dopant could also be seen from the XRD patterns. The (311) diffraction peaks of as-synthesized samples are shown in Fig. S2 (ESI†). The (311) peaks shift to lower 2 theta angles with increasing the Zn dopant concentration, indicating the enlargement of the lattice constants. The as-observed irregular shape and poor

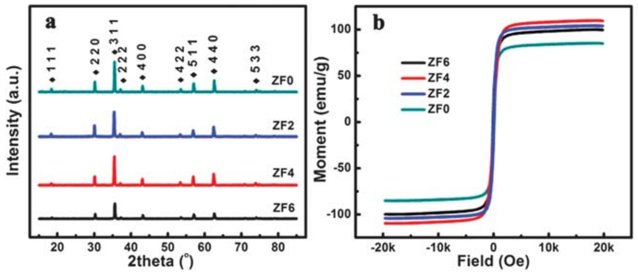

Fig. 3 (a) Typical XRD patterns and (b) magnetic hysteresis loops of Zn ferrite samples.

crystallinity of samples ZF6 and ZF7 may account for the abnormal decrease of lattice constant with increasing Zn dopant concentration.

We further investigated the magnetic properties of as-synthesized zinc ferrite NPs. The room temperature magnetic hysteresis (M-H) loops were collected and the saturation magnetization (M_s) values were recorded, as shown in Table 1. The M-H loops of some typical samples are shown in Fig. 3b. Actually, sample ZF0 is pure Fe_3O_4 without any zinc dopant, while ZF1 to ZF7 are zinc doped ferrite samples. Sample ZF0, which shows a normal magnetization of bulk Fe_3O_4, *i.e.* 83.5 emu g^{-1}, while samples with numbers from ZF2 to ZF5 exhibit much higher M_s. Sample ZF4 with the composition of $Zn_{0.468}Fe_{2.532}O_4$ shows the maximum M_s of 110 emu g^{-1}. Empirical analysis leads us to assume that this high magnetization of zinc dopant ferrite NPs is mainly caused by the non-stoichiometric structure, as it could lead to a redistribution of iron atoms in the tetrahedral sites and octahedral sites. Hence, a question is raised here, *i.e.* how do the zinc and iron atoms distribute in the spinel structure? To settle this question, Mössbauer spectra were employed to acquire more details on the magnetic structure of as-synthesized zinc ferrite samples.

Mössbauer spectra recorded at ambient conditions are displayed in Fig. 4a. The presence of two sextets in all samples confirms that the room temperature ferrimagnetism is shown not only by pure Fe_3O_4 (ZF0) but also by Zn doped ferrite samples. As is known, Fe_3O_4 owns an inverse spinel structure,[48] in which half of the Fe^{3+} cations occupy tetrahedral (A) sites, while all of the Fe^{2+} cations and the other half of the Fe^{3+} cations occupy octahedral (B) sites, resulting in the structural formula of $[Fe^{3+}]_A[Fe^{3+}Fe^{2+}]_BO_4$. The Mössbauer spectra were suitably fitted by two well-defined sextets, corresponding to Fe ions at A sites and B sites, and the relative areas of the subspectra for A and B sites are assumed to be proportional to the number of Fe cations occupying these sites.[49] From the fitting results, the absorption area ratio of A site to B site subspectra for sample ZF0 is 0.52, indicating that the Fe ions' distribution in as-synthesized Fe_3O_4 is very close to the standard material. With the amount of zinc dopant getting lager, the area ratio for Fe_A (Fe ions at A site) over Fe_B decreased correspondingly, as showed by the experimental values in Fig. 4b. The error bars in the experimental results represent the evaluation error during the measurement and the fitting process. The results may allow us to speculate that the zinc dopant will lead to a reduction of Fe ions at A sites or an increase of Fe ions in B sites. The former speculation seems more reliable in our case, that is to say, the replacement of some Fe atoms at A sites by Zn atoms is probable. And here we assume that this replacement exists only at A sites first. Correspondingly, the formula is described as $[Zn^{2+}{}_dFe^{3+}{}_{1-d}]_A[Fe^{3+}{}_{1+d}Fe^{2+}{}_{1-d}]_BO_4$ and used for further analysis. As previously introduced, d stands for the concentration of zinc dopant. In order to shed some light on the locations of Zn atoms, theoretically predicted ratios of Fe_A to Fe_B were gained by working out $(1-d)/2$. These theoretically predicted ratios according to Zn dopant concentrations are also shown in Fig. 4b by the red dashed line. If all the doped Zn atoms were at A sites, the ratio of Fe_A to Fe_B *versus* d values would follow the dashed line. As we can see, the line shows a clear trend that the ratio of Fe_A to Fe_B decreases with increasing the Zn dopant concentration. This trend is very close to the one estimated from Mössbauer measurements. If there were some Zn cations substituting into B sites, the predicted ratio of Fe_A to Fe_B would be above the red dashed line. This is contrary to the acquired results from Mössbauer spectra. Therefore, the assumption that Zn ions only substitute Fe ions at A sites is reasonable. In terms of Néel's theory,[50] the partial substitution of Fe^{3+} cations at A sites by non-magnetic atoms will result in an enhancement of the net moment from 4 μ_B per unit formula (for Fe_3O_4) to higher values, which is consistent with our results. All Zn ferrite samples show higher magnetizations than the as-prepared Fe_3O_4 sample. The low chemical synthesis temperature (here 280 °C) may account for the stable distribution of Zn atoms at A sites, according to Arean's work,[51] the inversion degree of Fe atoms increases with the decrease of equilibrium temperature. Our XPS analysis on the valence change of iron ions with Zn dopant concentration further testified the assumption of the preferred occupation of Zn atoms at A sites.

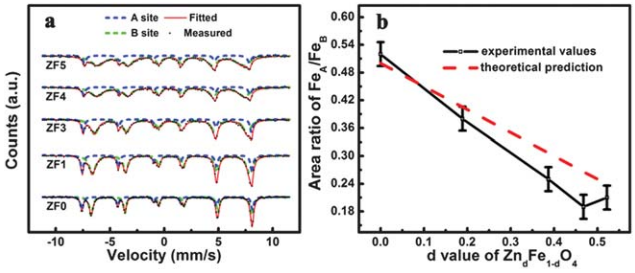

Fig. 4 (a) The Mössbauer spectra of Zn ferrite samples and fitted curves; (b) variation of area ratio of Fe_A to Fe_B *versus* Zn dopant concentration d. The experimental values are evaluated from the fitting results of Mössbauer spectra, while the red dashed line follows $Fe_A/Fe_B = (1-d)/2$.

Application as radar absorber materials (RAMs)

Microwave absorption performance has been reported to be related to particle size and shape.[52] Hence, to make a comparison with Fe_3O_4 (sample ZF0), sample ZF2 was selected. As seen from Fig. 1a and c, these two samples have similar size and shape, but with different compositions. Sample ZF2 with a nominal composition of $Zn_{0.290}Fe_{2.710}O_4$ shows a relatively high M_s of 106.8 emu g^{-1} compared with sample ZF0.

The acquired electromagnetic parameters (ε', ε'', μ', and μ'') of as-measured samples in the frequency range of 0.1 to 18 GHz are shown in Fig. 5a and b. There is not much difference between the permittivity (ε' and ε'') of samples ZF0 and ZF2, while obviously different trends are observed in their permeability (μ' and μ''). A single resonance peak is shown by ZF0. The real part of permeability decreases sharply when the frequency is above 1 GHz. At this point, the imaginary part of permeability starts to increase, then reaches a maximum value of 0.8 at 1.55 GHz, and finally decreases severely to almost zero after 12 GHz. An obviously different result was observed for zinc ferrite. Multi-resonance peaks exist in the measured frequency range. Three

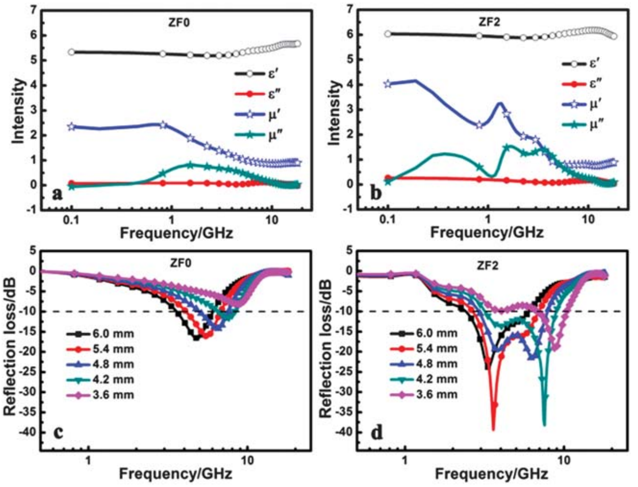

Fig. 5 (a) and (b) are the permittivity (ε', ε'') and permeability (μ', μ'') spectra; (c) and (d) are the calculated frequency dependent reflection loss plots. The measurements are performed in the frequency range of 0.1 to 18 GHz.

peaks of the imaginary part of permeability appear at 0.36 GHz, 1.67 GHz and 3.45 GHz, corresponding to intensities of 1.23, 1.68 and 1.42. As revealed by Srivastava,[32] the permeability spectrum is related to domain structures. Further investigations on the multi resonant peaks are underway based on the micromagnetics and will be described elsewhere.

As observed, an enhancement of the imaginary part of permeability μ'' together with shifted resonant peaks to higher frequency range were brought about by zinc ferrite NPs. μ'' is commonly used to present the magnetic loss caused by magnetic particles,[33] and even a small variation of μ'' may make a great change to the microwave absorption performance, which could be revealed by the calculated reflection loss (RL) by using the measured electromagnetic parameters. The reflection loss corresponding to a value of -10 dB is always used as a criterion, which means that 90% of the incident microwave is absorbed.[53] From the frequency dependent RL curves in Fig. 5c and d, we could see a distinct improvement brought about by the zinc ferrite sample. The thickness of as-made absorbers plays an important role in the microwave absorption performance. An optimal thickness will render the RL value at the resonant frequency as low as possible. For sample ZF2, two optimal thicknesses could be observed due to its multi-resonance peaks of permeability. One is 4.2 mm, corresponding to a RL value of -38 dB at a relatively high frequency of 7.5 GHz. The frequency band with RL values exceeding -10 dB is about 5.83 GHz. The other is 5.5 mm, corresponding to a RL value of -39.4 dB at a relatively low frequency of 3.6 GHz. These results are remarkable in the spinel ferrites, such as Fe_3O_4[54] and Ni–Zn ferrites,[55] and even competitive with the alloys.[56] Therefore, Zn ferrite NPs obtained in this work are attractive candidates for radar absorptive materials.

Synthesis and characterizations of small zinc ferrite NPs

For the purpose of biomedical applications, we have also synthesized Zn ferrite NPs with relatively small sizes by scaling down the iron and zinc precursors. To keep the composition of the as-synthesized zinc ferrite, the ratio of the iron to zinc precursors was fixed at 2 : 1. The amount of the precursors was scaled down from 18 mmol [12 mmol of $Fe(acac)_3$ + 6 mmol of $Zn(acac)_2$] to 12 mmol [8 mmol of $Fe(acac)_3$ + 4 mmol of $Zn(acac)_2$], then to 10.8 mmol [7.2 mmol of $Fe(acac)_3$ + 3.6 mmol of $Zn(acac)_2$]. Therefore three different sizes, 102.2 nm, 26.5 nm and 13.4 nm, were obtained and are shown in Fig. 6. Correspondingly, the samples were named as ZF3_102.2, ZF3_26.5 and ZF3_13.4. The corresponding size distributions were obtained by measuring the average diameters of 100–120 NPs in the SEM images or TEM images. Especially for the small particles, the size distribution is remarkably narrow, as indicated by the size histograms (Fig. 6). As seen from the VSM results in Fig. 7a, the saturation magnetization decreases considerably with the particles size getting smaller; only 30 emu g^{-1} for 13 nm Zn ferrite NPs. The great disorder of surface spin may become dominant due to the large specific surface area of the small particles, leading to the substantial reduction of magnetization.[57,58] As seen from the M–H loops, 102.2 nm Zn ferrite particles with a coercivity of 38 Oe (inset of Fig. 7a) were characterized to be ferromagnetic. When the particle size decreased to 13.2 nm, room temperature superparamagnetism was revealed by the FC (field cooled) and ZFC (zero field cooled) curves (lower lines in Fig. 7b). The blocking temperature of 13.4 nm Zn ferrite particles was around 160 K. While for 26.5 nm Zn ferrite particles, the FC–ZFC plots (upper lines in Fig. 7b) displayed a blocking temperature slightly below 300 K, as determined from the intersection of the ZFC data and FC data. But a non-zero coercivity (7 Oe) was observed from the M–H loop. Hence we defined the particles to be quasi-superparamagnetic at room temperature.

In this work, Zn ferrite NPs with relatively small sizes were purposely synthesized for biomedical applications, which usually require a magnetic NPs system to possess high M_s, low toxicity, good dispersibility and colloidal stability.[59] Although sample ZF3_102.2 shows a very high M_s of about 107 emu g^{-1}, it is not suitable for biomedical applications because the particles are difficult to disperse into aqueous solution. The particles could be dispersed into oleic acid for the measurement of

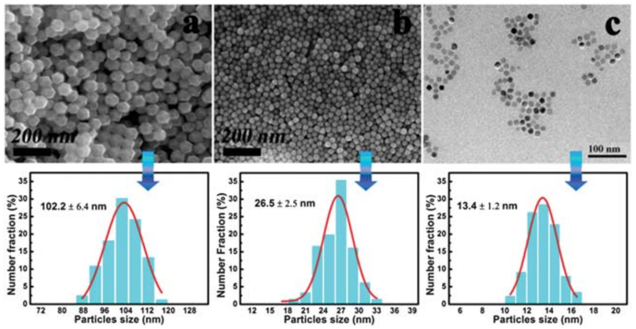

Fig. 6 (a) and (b) are the SEM images of samples with different sizes and corresponding size distribution histograms. The error bar means particle size deviation from the average value. (c) The TEM image and corresponding size distribution histogram for 13.4 nm Zn ferrite NPs.

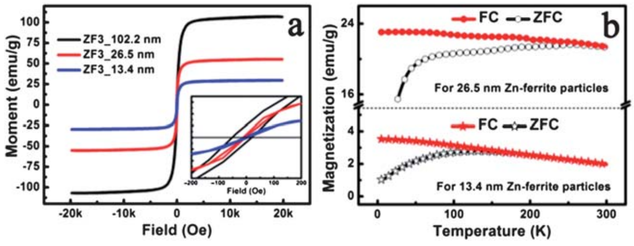

Fig. 7 (a) Magnetic hysteresis loops for 102.2 nm, 26.5 nm and 13.4 nm Zn ferrite NPs. The inset shows the coercivity. (b) FC–ZFC curves measured under an applied field of 100 Oe. The upper and lower lines are for 26.5 nm and 13.4 nm Zn ferrite NPs, respectively.

dynamic light scattering, and the result is shown in Fig. S3 (ESI†). Hence, further improvement of the dispersibility of large size Zn ferrite particles in aqueous solution should be made before they are applied into bioengineering. In this work, sample ZF3_26.5 with a saturation magnetization of 56 emu g^{-1} was selected as hyperthermia agent.

Provided that the precursors were scaled up to 24 mmol [16 mmol $Fe(acac)_3$ and 8 mmol $Zn(acac)_2$] for a larger particle size, the formed Zn ferrite NPs become irregular as in sample 7, as shown by the SEM image in Fig. S4 (ESI†). This also evidences that the reasonable precursor/surfactant ratio should be under 0.85 in the developed synthesis method. That is why we use 12 mmol of Fe precursor as starting material for the study on synthesis of Zn ferrites.

The cytotoxicity test and application on magnetic fluid hyperthermia (MFH)

Prior to being used as hyperthermia agent, the surface of 26.5 nm zinc ferrite NPs was modified by synthesized P-mPEG. An intensive study has been reported by our group[37] on the heating ability of P-mPEG coated Fe_3O_4 NPs. Similar experimental conditions are adopted in the current work. For a better understanding of the properties of as-synthesized zinc ferrites, the studies on cytotoxicity and heating efficiency were developed by comparison with the previously reported one.

Fig. 8a shows the FTIR spectra of oleic acid and P-mPEG coated Zn ferrite particles in the wave-number range between 400 and 4000 cm^{-1}. A metal–oxygen band at around 590 cm^{-1} could be observed in both spectra, which corresponds to the intrinsic lattice vibrations of tetrahedral coordination compound in the spinel structure.[60] The bands with peaks around 1630 and 3450 cm^{-1} were characteristic of the symmetric ν_s(COO–) stretch and O–H stretching vibrations, respectively.[61] In the FT-IR spectrum of P-mPEG coated Zn ferrite nanoparticles, the P–O stretching vibration was observed at around 1012 cm^{-1}. The band with a peak at 840 cm^{-1} was assigned to the vibration of the C–C ring.[62] The asymmetric ν_s(COC) stretch of methacryloyloxy group was positioned at 1104 cm^{-1}. The bands at around 1385 and 2903 cm^{-1} were attributed to the CH_3 and CH_2 stretching vibrations,[63] respectively. Besides, the characteristic bands such as the bands at 1466, 1354, 1300 and 1250 cm^{-1} are also observed for modified Zn ferrite NPs. This FT-IR analysis was very useful for evidencing the capping of P-mPEG on the surface of Zn ferrite NPs.

The coating of P-mPEG on the surface of zinc ferrite NPs could further be confirmed by the TEM image, as shown by the inset of Fig. 8b. A contrast difference between the surface coating and core NPs was clearly observed. After the surface coating, the hydrophobic zinc ferrite NPs were successfully transferred into a water phase. The modified NPs are well dispersed in aqueous solution and the average hydrodynamic size (Fig. 8b) examined by dynamic light scattering (DLS) is *ca.* 38.2 nm. This indicates that the used P-mPEG surface coating effectively prevents the particles from agglomerating in the aqueous solution.

To evaluate the cytotoxicity of the modified zinc ferrite and Fe_3O_4 NPs (similar size, as in a previous report[37]), we performed a standard CKK viability test on MCF-7 cancer cells after 24 h incubation with the magnetic NPs at various incubation concentrations (5–200 Fe μg mL^{-1}). The viability profiles of cells treated with two different NPs, as shown in Fig. 9, reveals that almost 90% cell viability is achieved after cells were incubated for 24 h with 200 Fe μg mL^{-1} of zinc ferrite NPs. As for cells treated with Fe_3O_4 NPs, the viability decreases gradually with Fe concentration and only 65% cell viability is maintained when 200 Fe μg mL^{-1} of Fe_3O_4 NPs are used. The good cytocompatibility exhibited by as-synthesized zinc ferrite NPs makes them superior for biomedical applications.

The characterization of heat dissipation of zinc ferrite NPs was performed on an induction heating system (Ambrell, Easy Heat, 4.2–10 kW). As detected by the ICP-MS analysis, the zinc ferrite NPs dispersed in water are at a Fe concentration of

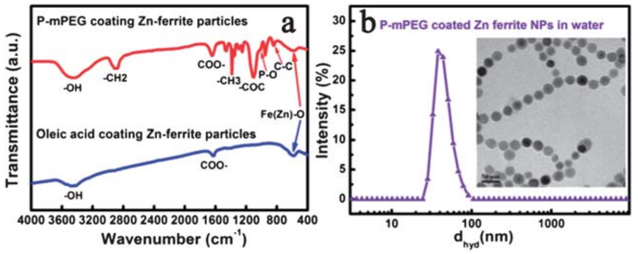

Fig. 8 (a) FTIR spectra of 26.5 nm Zn ferrite NPs before and after surface modification by P-mPEG. (b) Dynamic light scattering (DLS) of the aqueous suspension of P-mPEG coated 26.5 nm Zn ferrite NPs and the TEM image (inset).

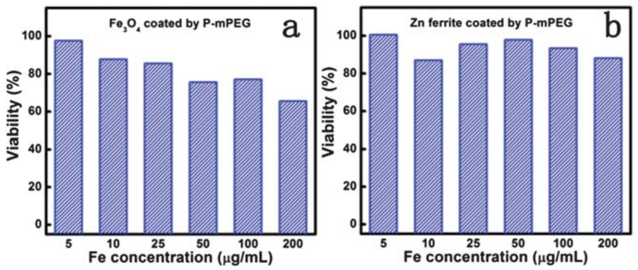

Fig. 9 Viability test results of MCF-7 cancer cells with (a) modified 19 nm Fe_3O_4 and (b) 26.5 nm Zn ferrite after incubation for 12 h.

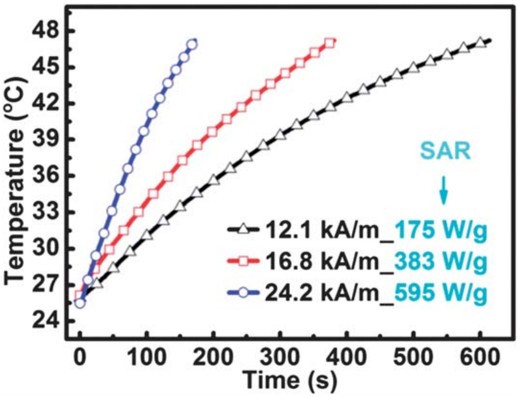

Fig. 10 The temperature–time curves of P-mPEG coated zinc ferrite dispersed in water and the corresponding SAR values. The heating efficiency measurement was performed under an alternative magnetic field with a frequency of 240 kHz.

1.2 mg mL^{-1}. Due to the Zn^{2+} ions being non-magnetic, herein only Fe concentration is taken into consideration and adopted for the estimate of SAR values. The temperature–time curves in Fig. 10 were recorded when samples were exposed to an AMF field of 12.1–24.2 kA m^{-1} (*i.e.* 150–300 Oe) at a frequency of 240 kHz. As characterized by eqn (3), SAR values obtained according to the initial temperature rise vary from 175 W g^{-1} to 595 W g^{-1}, depending on the applied AFM field strength. The higher the field strength, the larger the SAR value is. Hence the as-defined ESAR value is preferred to be used to evaluate the heat efficiency of modified magnetic NPs. As calculated according to the definition of ESAR, the average and optimal ESAR values are 31.4×10^{-9} W g^{-1} Oe^{-2} Hz^{-1} and 36×10^{-9} W g^{-1} Oe^{-2} Hz^{-1}, respectively. The reference works on commonly used hyperthermia agents,[64–68] such as Fe_3O_4, $MnFe_2O_4$ and $CoFe_2O_4$ were investigated to make a comparison. The reported ESAR values are mostly in the range of 13.6×10^{-9} to 33.8×10^{-9} W g^{-1} Oe^{-2} Hz^{-1}. Among those reported works, the high ESAR value of our sample is noticeable, which may originate from the high M_s and narrow size distribution of the as-synthesized zinc ferrite particles. The heat generation by the employed zinc ferrite sample could be due to Néel and Brownian loss,[69] which mainly arise from the rotation of the magnetization vector and the self-rotation of NPs when positioned in an external alternating magnetic field, while the hysteresis loss might be ignored for the tiny coercivity of the NPs. Apparently, the good biocompatibility combined with high heating efficiency makes P-mPEG Zn ferrite NPs have potential use for *in vivo* trials on cancer therapy.

Conclusion

In the present work, we demonstrate a novel controlled synthesis of non-stoichiometric zinc ferrite NPs, which possess extraordinary magnetism at room temperature. The composition of as-synthesized zinc ferrites could be controlled well by the molar ratio of Zn to Fe precursors. We could discriminate Fe and Zn precursors as primary and secondary precursors due to their parts in the synthesis. As we found, the ratio of surfactant/Fe precursor is more decisive in the particle size, while the further addition of Zn precursor plays an important role in the resultant composition as well as the morphology of the NPs. Through the studies on the effects of composition, lattice structure as well as hyperfine magnetic structure on the magnetization of as-synthesized zinc ferrite NPs, we could build a formula model for our sample, *i.e.* $[Zn^{2+}{}_{d}Fe^{3+}{}_{1-d}]_A[Fe^{3+}{}_{1+d}Fe^{2+}{}_{1-d}]_BO_4$. The partial occupation of Fe^{3+} cations at A sites may account for the extra high saturation. The unusual magnetism and uniform particle size make the as-synthesized zinc ferrites quite attractive as radar absorption materials. Multi-resonance peaks shown by the permeability spectra result in effective reflection losses in the GHz frequency band. When the composition is decided by fixing the ratio of Zn to Fe precursor, the particle size could further be tuned by scaling down the amounts of Fe and Zn precursors. We successfully synthesized Zn ferrite NPs with sizes of 26.5 nm and 13.4 nm, of which the Zn dopant concentration is around $d = 0.38$. The decrease of particle size makes a great impact on the resultant magnetization, which may result from the relatively large surface/volume ratio in smaller particles, which makes spin canting on the surface more competitive to the intra-ferromagnetic moments. In spite of this, Zn ferrite NPs with a size of 26.5 nm show a magnetization as high as 55 emu g^{-1} and were selected for hyperthermia agents. Prior to the hyperthermia application, a surface coating layer of P-mPEG was employed to provide dispersibility and biocompatibility. The modified Zn ferrite NPs are much safer than Fe_3O_4, which is a kind of popular hyperthermia agent in studies. In view of the heating efficiency produced by magnetic NPs, our samples are very remarkable and show tremendous potential in biomedical applications.

Acknowledgements

This work was supported by Ministry of Education (MOE) Academic Research Fund of Singapore under Grants-MOE2011-T2-1-043 (R284-000-097-112) and A*Star SERC (R294-000-105-305).

Notes and references

1 A. Goldman, *Modern Ferrite Technology*, Springer, Pittsburgh, PA, USA, 2nd edn, 2006, p. 353.

2 D. L. Zhao, Q. Lv and Z. M. Shen, *J. Alloys Compd.*, 2009, **480**, 634–638.

3 N. Velinov, E. Manova, T. Tsoncheva, C. Estournès, D. Paneva, K. Tenchev, V. Petkova, K. Koleva, B. Kunev and I. Mitov, *Solid State Sci.*, 2012, **14**, 1092–1099.

4 A. K. Gupta and M. Gupta, *Biomaterials*, 2005, **26**, 3995–4021.

5 Z. Beji, A. Hanini, L. S. Smiri, J. Gavard, K. Kacem, F. Villain, J. M. Grenèche, F. Chau and S. Ammar, *Chem. Mater.*, 2010, **22**, 5420–5429.

6 G. F. Dionne, *Magnetic Oxides*, Springer-Verlag, LLC., New York, 1st edn, 2009, p. 152.

7 J. T. Elizalde Galindo, A. H. Adair, C. E. Botez, V. Corral Flores, D. Bueno Baques, L. Fuentes Cobas and

J. A. Matutes Aquino, *Appl. Phys. A: Mater. Sci. Process.*, 2007, **87**, 743–747.

8 B. Pandey and H. C. Verma, *Hyperfine Interact.*, 2008, **183**, 17–24.

9 B. K. Nath, P. K. Chakrabarti, S. Das, U. Kumar, P. K. Mukhopadhyay and D. Das, *Eur. Phys. J. B*, 2004, **39**, 417–425.

10 W. B. Cross, L. Affleck, M. V. Kuznetsov, I. P. Parkin and Q. A. Pankhurst, *J. Mater. Chem.*, 1999, **9**, 2545–2552.

11 R. W. Grimes, A. B. Anderson and A. H. Heuer, *J. Am. Chem. Soc.*, 1989, **111**, 7–15.

12 J. M. Hastings and L. M. Corlliss, *Phys. Rev.*, 1956, **102**, 1460–1463.

13 V. B. Gutiérrez, M. J. T. Fernández and R. S. Puche, *J. Phys. Chem. C*, 2010, **114**, 1789–1795.

14 S. A. Oliver, V. G. Harris, H. H. Hamdeh and J. C. Ho, *Appl. Phys. Lett.*, 2000, **76**, 2761–2763.

15 S. Ammar, N. Jouini, F. Fiévet, O. Stephan, C. Marhic, M. Richard, F. Villain, C. C. D. Moulin, S. Brice and P. Sainctavit, *J. Non-Cryst. Solids*, 2004, **345–346**, 658–662.

16 J. T. Jang, H. Nah, J. H. Lee, S. H. Moon, M. G. Kim and J. Cheon, *Angew. Chem., Int. Ed.*, 2009, **48**, 1234–1238.

17 T. M. Clark and B. J. Evans, *IEEE Trans. Magn.*, 1997, **33**, 3745–3747.

18 F. J. Burghart, W. Potzel, G. M. Kalvius, E. Schreier, G. Grosse, D. R. Noakes, W. Schäfer, W. kockelann, S. J. Campbell, W. A. Kaczmarek, A. Martin and M. K. Krause, *Phys. B*, 2000, **289–290**, 286–290.

19 C. N. Chinnasamy, A. Narayanasamy, N. Ponpandian, K. Chattopadhyay, H. Guérault and J. M. Greneche, *J. Phys.: Condens. Matter*, 2000, **12**, 7795–7805.

20 K. Suresh, N. R. S. Kumar and K. C. Patil, *Adv. Mater.*, 1991, **3**, 148–150.

21 D. Makovec and M. Drofenik, *J. Nanopart. Res.*, 2008, **10**, 131–141.

22 V. B. Gutiérrez, F. J. Villacorta, P. Bonville, M. J. T. Fernández and R. S. Puche, *J. Phys. Chem. C*, 2011, **115**, 1627–1634.

23 Y. Lin, W. Yao, Y. Cheng, H. Q. Qian, X. Wang, Y. Ding, W. Wu and X. Q. Jiang, *J. Mater. Chem.*, 2012, **22**, 5684–5693.

24 Y. T. Li, Q. Li, M. L. Wen, Y. Zhang, Y. Zhai, Z. Xie, F. Q. Xu and S. Q. Wei, *J. Electron Spectrosc. Relat. Phenom.*, 2007, **160**, 1–6.

25 J. Liu, Y. Z. Bin and M. Matsuo, *J. Phys. Chem. C*, 2012, **116**, 134–143.

26 J. P. Singh, R. C. Srivastava, H. M. Agrawal and R. P. S. Kushwaha, *Hyperfine Interact.*, 2008, **183**, 221–228.

27 M. Hofmann, S. J. Campbell, H. Ehrhardt and R. Feyerherm, *J. Mater. Sci.*, 2004, **39**, 5057–5065.

28 M. P. Morales, S. V. Verdaguer, M. I. Montero and C. J. Serna, *Chem. Mater.*, 1999, **11**, 3058–3064.

29 J. Park, K. An, Y. Hwang, J. G. Park, H. J. Noh, J. Y. Kim, J. H. Park, N. M. Hwang and T. Hyeon, *Nat. Mater.*, 2004, **3**, 891–895.

30 F. Fausto, *Characterization and Measurement of Magnetic Materials*, Academic Press, Amsterdam, 1st edn, 2004, p. 69.

31 S. A. Popescu, P. Vlazan, S. Novaconi, O. Grozescu and P. V. Notingher, *U. P. B. Sci. Bull., Series C*, 2011, **73**, 247–256.

32 C. M. Srivastava, S. N. Shringi, R. G. Srivastava and N. G. Nanadikar, *Phys. Rev. B: Solid State*, 1976, **14**, 2032–2040.

33 A. G. Yan, X. H. Liu, R. Yi, R. R. Shi, N. Zhang and G. Z. Qiu, *J. Phys. Chem. C*, 2008, **112**, 8558–8563.

34 Y. B. Li, R. Yi, A. G. Yan, L. W. Deng, K. C. Zhou and X. H. Liu, *Solid State Sci.*, 2009, **11**, 1319–1324.

35 P. Chandrasekharan, D. Maity, C. X. Yong, K. H. Chuang, J. Ding and S. S. Feng, *Biomaterials*, 2011, **32**, 5663–5672.

36 L. Li, Y. Yang, J. Ding and J. M. Xue, *Chem. Mater.*, 2010, **22**, 3183–3191.

37 X. L. Liu, H. M. Fan, J. B. Yi, Y. Yang, E. S. G. Choo, J. M. Xue, D. D. Fan and J. Ding, *J. Mater. Chem.*, 2012, **22**, 8235–8244.

38 U. I. Tromsdorf, O. T. Bruns, S. C. Salmen, U. Beisiegel and H. Weller, *Nano Lett.*, 2009, **9**, 4434–4440.

39 Y. Yang and J. Ding, *J. Alloys Compd.*, 2012, **528**, 58–62.

40 B. Jeyadevan, *J. Ceram. Soc. Jpn.*, 2010, **118**, 391–401.

41 W. X. Niu, S. L. Zheng, D. W. Wang, X. Q. Liu, H. J. Li, S. Han, J. Chen, Z. Y. Tang and G. B. Xu, *J. Am. Chem. Soc.*, 2009, **131**, 697–703.

42 W. G. Lu, Q. S. Liu, Z. Y. Sun, J. B. He, C. Ezeolu and J. Y. Fang, *J. Am. Chem. Soc.*, 2008, **130**, 6983–6991.

43 Y. L. Hou, Z. C. Xu and S. H. Sun, *Angew. Chem., Int. Ed.*, 2007, **46**, 6329–6332.

44 J. Cheon, N. J. Kang, S. M. Lee, J. H. Lee, J. H. Yoon and S. J. Oh, *J. Am. Chem. Soc.*, 2004, **126**, 1950–1951.

45 M. V. Kovalenko, M. I. Bodnarchuk, R. T. Lechner, G. Hesser, F. Schffler and W. Heiss, *J. Am. Chem. Soc.*, 2007, **129**, 6352–6353.

46 Z. L. Wang, *J. Phys. Chem. B*, 2000, **104**, 1153–1175.

47 C. Yang, J. J. Wu and Y. L. Hou, *Chem. Commun.*, 2011, **47**, 5130–5141.

48 G. F. Dionne, *Magnetic oxides*, Springer, New York, Dordrecht, Heidelberg, London, 1st edn, 2009, p. 169.

49 B. H. Liu, J. Ding, Z. L. Dong, C. B. Boothroyd, J. H. Yin and J. B. Yi, *Phys. Rev. B: Condens. Matter Mater. Phys.*, 2006, **74**, 184427.

50 F. Fausto, *Characterization and Measurement of Magnetic Materials*, Academic Press, Amsterdam, 1st edn, 2004, p. 69.

51 C. O. Arean, J. L. R. Blanco and M. C. T. Fernandez, *J. Chem. Soc., Faraday Trans.*, 1992, **88**, 321–324.

52 F. S. Wen, W. L. Zuo, H. B. Yi, N. Wang, L. Qiao and F. S. Li, *Phys. B*, 2009, **404**, 3567–3570.

53 Y. P. Duan, Y. Yang, H. Ma, S. H. Liu, X. D. Cui and H. F. Chen, *J. Phys. D: Appl. Phys.*, 2008, **41**, 125403.

54 X. A. Li, X. J. Han, Y. J. Tan and P. Xu, *J. Alloys Compd.*, 2008, **464**, 352–356.

55 J. C. Aphesteguy, A. Damiani, D. DiGiovanni and S. E. Jacobo, *Phys. B*, 2009, **404**, 2713–2716.

56 L. G. Yan, J. B. Wang, X. H. Han, Y. Ren, Q. F. Liu and F. S. Li, *Nanotechnology*, 2010, **21**, 095708.

57 S. Ammar, N. Jouini, F. Fiévet, Z. Beji, L. Smiri, P. Moliné, M. Danot and J. M. Grenèche, *J. Phys.: Condens. Matter*, 2006, **18**, 9055–9069.

58 V. B. Gutiérrez, E. U. Garrote, M. J. T. Fernández and R. S. Puche, *Chem. Mater.*, 2010, **22**, 6130–6137.

59 I. Sharifi, H. Shokrollahi and S. Amiri, *J. Magn. Magn. Mater.*, 2012, **324**, 903–915.

60 E. Karaoğlu, A. Baykal, H. Deligöz, M. Şenel, H. Sözeri and M. S. Toprak, *J. Alloys Compd.*, 2011, **509**, 8460–8468.

61 L. Zhang, R. He and H. C. Gu, *Appl. Surf. Sci.*, 2006, **253**, 2611–2617.

62 M. G. Naseri, E. B. Saion and A. Kamali, *ISRN Nanotechnol.*, 2012, 604241.

63 H. Ando, M. Nakahara and M. Yamamoto, *Langmuir*, 1996, **12**, 6399.

64 B. Samanta, H. H. Yan, N. O. Fischer, J. Shi, D. J. Jerry and V. M. Rotello, *J. Mater. Chem.*, 2008, **18**, 1204–1208.

65 M. Suto, Y. Hirota, H. Mamiya, A. Fujita, R. Kasuya, K. Tohji and B. Jeyadevan, *J. Magn. Magn. Mater.*, 2009, **321**, 1493–1496.

66 L. Y. Zhang, H. C. Gu and X. M. Wang, *J. Magn. Magn. Mater.*, 2007, **311**, 228–233.

67 G. Baldi, G. Lorenzi and C. Ravagli, *Process. Appl. Ceram.*, 2009, **3**, 103–109.

68 P. Pradhan, J. Giri, R. Banerjee, J. Bellare and D. Bahadur, *J. Magn. Magn. Mater.*, 2007, **311**, 208–215.

69 S. Mornet, S. Vasseur, F. Grasset and E. Duguet, *J. Mater. Chem.*, 2004, **14**, 2161–2175.